

# Vibrational properties of $\text{LiNb}_{1-x}\text{Ta}_x\text{O}_3$ mixed crystals

M. Rüsing,<sup>\*</sup> S. Sanna, S. Neufeld, G. Berth, W. G. Schmidt, and A. Zrenner

*Department Physik, Universität Paderborn, 33095 Paderborn, Germany*

H. Yu, Y. Wang, and H. Zhang

*State Key Lab of Crystal Materials, Shandong University, Jinan 250100, People's Republic of China*

(Received 21 March 2016; published 23 May 2016)

Congruent lithium niobate and lithium tantalate mixed crystals have been grown over the complete compositional range with the Czochralski method. The structural and vibrational properties of the mixed crystals are studied extensively by x-ray diffraction measurements, Raman spectroscopy, and density functional theory. The measured lattice parameters and vibrational frequencies are in good agreement with our theoretical predictions. The observed dependence of the Raman frequencies on the crystal composition is discussed on the basis of the calculated phonon displacement patterns. The phononic contribution to the static dielectric tensor is calculated by means of the generalized Lyddane-Sachs-Teller relation. Due to the pronounced dependence of the optical response on the Ta concentration, lithium niobate tantalate mixed crystals represent a perfect model system to study the properties of uniaxial mixed ferroelectric materials for application in integrated optics.

DOI: [10.1103/PhysRevB.93.184305](https://doi.org/10.1103/PhysRevB.93.184305)

## I. INTRODUCTION

Lithium niobate ( $\text{LiNbO}_3$ , LN) and lithium tantalate ( $\text{LiTaO}_3$ , LT) are uniaxial ferroelectric materials with Curie temperatures of 1483 and 838 K, respectively [1]. Both materials are characterized by a large spontaneous polarization (71 and 50  $\mu\text{C}/\text{cm}^2$ , respectively [1]) and are vastly employed for applications in linear and nonlinear integrated optics as well as surface acoustic wave generation [2]. In these applications, the unusual large piezoelectric, electro-optic, and nonlinear coefficients of the materials are exploited [3]. Both crystals are isostructural and crystalize below the Curie temperature in the space group  $R3c$  [4]. Due to the small ionic radius difference [5], Nb is easily substituted by the isoelectronic Ta, which allows for the fabrication of  $\text{LiNb}_{1-x}\text{Ta}_x\text{O}_3$  mixed crystals over the complete compositional range [6–8]. In contrast to semiconductor technology, where alloys are largely employed for property tailoring, the potential of ferroelectric alloys for applications in integrated optics is largely unexplored. Lithium niobate-tantalate (LNT) mixed crystals represent a prototypical example of such a material system. The most remarkable feature for applications in integrated optics is the possibility to tune the refractive index and the birefringence by adjusting the Nb/Ta ratio. Previous studies suggested the existence of a stoichiometry with no optical birefringence at room temperature in the range from  $x = 0.93$  to  $0.96$  [9,10]. The resulting material is an optically isotropic crystal that retains the exclusive advantages of ferroelectrics, such as the large electro-optic and nonlinear optical coefficients [7].

Despite these promising features, only a very few studies exist which deal with the properties of LNT mixed crystals. Previous experimental studies mainly focused on crystal growth and lattice parameters [6–8]. Moreover, the thermal expansion characteristics [6,7] as well as the Curie temperatures of the LNT system have been determined [7]. Theoretical work on LNT is even rarer. The linear and

nonlinear susceptibilities have been calculated for a few selected stoichiometric compositions based on the chemical bond method [11] or by *ab initio* theories [12]. Previously, we presented an *ab initio* study, which dealt with the lattice parameters of LNT crystals and the frequency of the phonon modes with  $A_1$  symmetry [13]. Based on our theoretical models, we suggested that the  $A_1$  transverse-optical (TO) zone-center phonon frequencies, which can be measured, e.g., by Raman spectroscopy, allow for the exact determination of the LNT stoichiometry.

In this work, we systematically study the compositional dependence of all Raman active phonon modes experimentally and by density functional theory. In order to perform Raman experiments over the complete compositional range, LNT mixed crystals have been grown by the Czochralski technique and characterized by x-ray diffraction (XRD) measurements. The phonon frequency shifts, as well as the lattice parameters, have been recorded as a function of the Ta concentration. Based on this data, the dielectric properties have been estimated using the well-established Lyddane-Sachs-Teller relation. The structure of this study is as follows: Sec. II deals with the crystal growth process, the experimental setup of the Raman measurements, and the methodology of the calculations. In Sec. III, the experimental and theoretical results are presented and discussed. The analysis closes in Sec. IV with a summary of the main results.

## II. METHODOLOGY

### A. Crystal growth

Mixed  $\text{LiNb}_{1-x}\text{Ta}_x\text{O}_3$  crystals can be obtained over the whole solid-solution range from pure LN to LT. To this end, LNT crystals have been grown by the Czochralski method [7]. The Czochralski growth results in congruent—i.e., lithium deficient—crystals with composition varying from 48.5 Li mole % in LN to 49 Li mole % in LT [14–16]. The initial charge for growing the single crystals was made from raw materials of commercial  $\text{LiNbO}_3$  and  $\text{LiTaO}_3$  powders with

<sup>\*</sup>michael.ruesing@upb.de

a chemical purity of 99.99%. The raw materials of the mixed crystals were synthesized by a solid-state reaction. The amounts of raw materials were weighed and combined with a  $\text{LiNbO}_3\text{:LiTaO}_3$  proportion of 0.125:0.875, 0.25:0.75, 0.375:0.625, and 0.625:0.375, respectively. Then the materials were ground, mixed for 10 h, and pressed into cylinders under high pressure. Single crystals were grown by the Czochralski method using an iridium crucible in nitrogen atmosphere. The apparatus used to heat the crucible was a 2 kHz low-radio-frequency furnace. Pure  $\text{LiNbO}_3$  single crystals along the  $z$  axis were used in the growth process as seeds. After dipping the seed into the melt and adjusting the heating power of the furnace, the crystal was pulled at a rate of 0.5–3.0 mm/h, with a rotation rate of 8 rpm. After the growth process was completed, the crystal was cooled to room temperature at a rate of 20 °C/h. Smaller samples have been cut from the grown crystals for further investigations. The phase identification of the as-grown crystals was performed using a Seifert x-ray powder diffractometer (XRPD) and  $\text{Cu-K}\alpha$  radiation at room temperature over a  $2\Theta$  range of 10–80°. Our set of LNT mixed crystals is complemented by the two end compounds LN and LT. Corresponding commercial samples have been grown by The Roditi International Corporation Ltd (LN) and by Döhner Elektrooptik GmbH (LT).

### B. Raman experiment

In their ferroelectric phase,  $\text{LiNbO}_3$  and  $\text{LiTaO}_3$  can be described by an orthorhombic unit cell containing two formula units [4]. This leads to 30 vibrational degrees of freedom. According to group theory, the optical phonon modes at the zone center can be further divided in four  $A_1$ , five  $A_2$ , and nine twofold-degenerated  $E$  phonons. The  $A_1$  and the  $E$  modes are Raman and infrared active, while the  $A_2$  branch is optical inactive. The infrared activity of those modes is associated with long-range electric fields leading to a lift of the degeneracy between longitudinal-optical (LO) and transverse-optical (TO) modes at the zone center [17–19]. Therefore, in total, 22 zone-center Raman modes are detectable.

The crystal structure of both LN and LT has  $C_{3v}$  symmetry [3] and the corresponding Raman tensors for the irreducible representations of the  $3m$  point group are given by [20]

$$\begin{aligned} A_1(z) &= \begin{pmatrix} a & 0 & 0 \\ 0 & a & 0 \\ 0 & 0 & b \end{pmatrix}, & E(y) &= \begin{pmatrix} c & 0 & 0 \\ 0 & -c & d \\ 0 & d & 0 \end{pmatrix}, \\ E(-x) &= \begin{pmatrix} 0 & -c & -d \\ -c & 0 & 0 \\ -d & 0 & 0 \end{pmatrix}. \end{aligned} \quad (1)$$

Here, the letter in brackets indicates the polarization of the respective phonon branch in crystal coordinates. In this study, the scattering geometry is described in Porto's notation:  $k_i(e_i, e_s)k_s$ . The vectors  $k_i$  and  $k_s$  mark the direction of the incident and scattered light in crystal coordinates, while  $e_i$  and  $e_s$  label its polarization. The intensity can be calculated for a given scattering configuration by  $I \propto |e_s R(x_n) e_i|^2$ , where  $R$  denotes the Raman tensor. For an unambiguous identification of all phonon modes in the mixed crystals, the Raman spectra have been taken in a complete set of backscattering geometries,

TABLE I. Observable phonon modes and Raman tensor elements for backscattering configurations.

Scattering configuration	Symmetry species	Tensor element	
		TO	LO
$x(y, y)\bar{x}$	$A_1\text{-TO}, E\text{-TO}$	$a^2 + c^2$	
$x(y, z)\bar{x}$	$E\text{-TO}$	$d^2$	
$x(z, y)\bar{x}$	$E\text{-TO}$	$d^2$	
$x(z, z)\bar{x}$	$A_1\text{-TO}$	$b^2$	
$y(x, x)\bar{y}$	$A_1\text{-TO}, E\text{-LO}$	$a^2$	$c^2$
$y(x, z)\bar{y}$	$E\text{-TO}$	$d^2$	
$y(z, x)\bar{y}$	$E\text{-TO}$	$d^2$	
$y(z, z)\bar{y}$	$A_1\text{-TO}$	$b^2$	
$z(x, x)\bar{z}$	$A_1\text{-LO}, E\text{-TO}$	$c^2$	$a^2$
$z(x, y)\bar{z}$	$E\text{-TO}$	$c^2$	
$z(y, x)\bar{z}$	$E\text{-TO}$	$c^2$	
$z(y, y)\bar{z}$	$A_1\text{-LO}, E\text{-TO}$	$c^2$	$a^2$

i.e., with  $k_i = -k_s$ . The scattering geometries and observable tensor elements are summarized in Table I.

The vibrational properties were analyzed on a  $\mu$ -Raman setup at room temperature. The excitation source (frequency-doubled Nd:YAG at 532 nm, 50 mW output) was focused on the samples via an infinity corrected objective with a numerical aperture (NA) of 0.55. No confocal pinhole was applied to assure a large scattering volume. The scattered light was collected through the same objective, analyzed in a single-stage spectrometer with an integrated Notch filter (KOSI f/1.8i), and detected with an attached Andor Newton BI CCD camera. The corresponding spectral resolution is about 2.3  $\text{cm}^{-1}$ . A more detailed description of the experimental setup can be found in Refs. [21,22].

### C. Computational methods

Lattice parameters and phonon frequencies of LNT mixed crystals have been modeled within the density functional theory. Total-energy and frozen phonon calculations are performed with the Vienna ab initio simulation package (VASP) [23] using the PW91 formulation [24] of the generalized gradient approximation (GGA) [25]. Thereby we have employed projector augmented-wave (PAW) potentials [26] with projectors up to  $l = 3$  for Nb and Ta, and  $l = 2$  for Li and O. The electronic wave functions are expanded into a plane-wave basis up to a kinetic energy of 400 eV.

A  $\Gamma$ -centered  $k$ -point mesh as large as  $8 \times 8 \times 8$  was used to carry out the integration in the Brillouin zone. Equilibrium geometries are obtained relaxing the atomic positions until the Hellman-Feynman forces acting on each atom are lower than 10 meV/Å. Lattice parameters are evaluated calculating the ground-state energy for fixed volumes and varying the latter by  $\pm 5\%$  around its experimental equilibrium value. The obtained energy surface as a function of the cell volume is then fitted to the Murnaghan equation of state [27],

$$E(V) = V_0 \frac{B}{B'} \left[ \frac{1}{B' - 1} \left( \frac{V_0}{V} \right)^{B' - 1} + \frac{V}{V_0} \right] + \text{const}, \quad (2)$$

where  $B$  is the bulk modulus,  $B'$  is its derivative with respect to the pressure, and  $V_0$  is the equilibrium volume. After obtaining  $V_0$  and adjusting the cell volume accordingly, the cell parameters are evaluated by a further relaxation, allowing both atomic positions and cell shape to relax. This approach allows one to reproduce the measured hexagonal lattice parameters  $a$  and  $c$  of the  $\text{LiNb}_{1-x}\text{Ta}_x\text{O}_3$  structure as well as the internal parameters  $z$ ,  $u$ , and  $w$  of the end compounds LN and LT within 1–2% of the measured values [4,8]. Forty-atom supercells consisting of a  $2 \times 2 \times 1$  repetition of the rhombohedral primitive unit cell allow for the simulation of the Ta concentration in multiples of 12.5%. The phonon mode frequencies and eigenvectors are calculated using the frozen phonon approach at the system's equilibrium geometry.

As a computational approach beyond density functional theory (DFT) is necessary for an accurate modeling of the material's optical response [12], we calculate the dielectric constants of the mixed crystals within hybrid DFT. Thereby the electron exchange and correlation energy is modeled with the Hyde-Scuseria-Ernzerhof (HSE06) screened hybrid functional [28,29], in which 25% of the local Perdew-Burke-Ernzerhof (PBE) exchange [30] is substituted by exact exchange.

The influence of the cation distribution in the mixed crystals on energetics, geometries, and phonon modes is accounted for in an approximate manner by averaging over the different configurations realizable with our supercells. Thus, our calculations neglect the influence of local stoichiometry fluctuations and model compositionally homogeneous crystals. Moreover, we did not take into account the lithium deficiency of congruent samples and the related intrinsic defects in our simulation. The calculation of the vibrational properties of the large supercells required for a proper treatment of the congruent composition [31–34] is beyond our computational means. However, our calculations on stoichiometric crystals reproduce, at least qualitatively, the experimental data.

### III. RESULTS

#### A. XRD characterization and lattice parameters

The XRD spectra of the samples are depicted in Fig. 1. The sharp peaks, which can be indexed in perfect accordance with the standard JCPDS Card File 38-1252 for  $\text{LiNb}_{0.5}\text{Ta}_{0.5}\text{O}_3$ , confirm that the as-grown crystals are well formed. Based on the XRD analysis, we have determined the hexagonal lattice parameters  $c$  and  $a$  of our samples, which are summarized in Table II. The real sample stoichiometry, however, must be carefully determined, as it might differ from the melt composition. Indeed, previous studies have shown that Czochralski-grown LNT crystals are Ta rich [6–9], meaning that the actual tantalum percentage  $x = \text{Ta}/(\text{Ta} + \text{Nb})$  in the crystals is larger than the corresponding nominal value  $y$  in the melt. As the exact knowledge of the compound stoichiometry is crucial for the interpretation of XRD and Raman analysis, a method has to be found to determine the Ta ratio  $x$  in the crystals. The LNT lattice parameter  $c$ , for example, depends heavily on the crystal stoichiometry and can therefore be used to calibrate the crystal composition [8].

Bartasyte *et al.* have established a relationship between the lattice parameter  $c$  of congruent LNT crystals and their

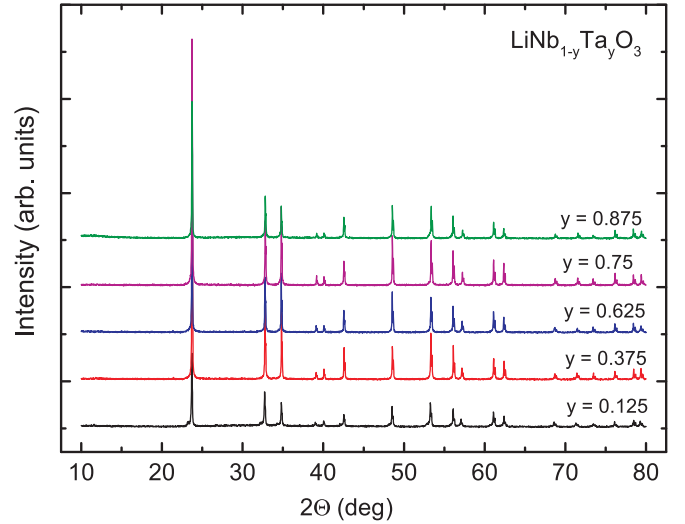


FIG. 1. Room-temperature XRD spectra over a  $2\Theta$  range of  $10$ – $80^\circ$  for all grown samples. All peaks can be indexed in accordance with the Joint Committee on Powder Diffraction Standards (JCPDS) Card File 38-1252 for  $\text{LiNb}_{0.5}\text{Ta}_{0.5}\text{O}_3$ . The spectra are labeled by the Ta concentration  $y$  in the melt. For the sake of clarity, the plots have been separated by an artificial offset.

composition in a recent work [8]. They described the Ta ratio dependency  $x$  of the lattice parameters  $a$  and  $c$  with a quadratic function of the form

$$p(x) = xp_{\text{LT}} + (1 - x)p_{\text{LN}} + bx(1 - x). \quad (3)$$

Here,  $p$  stands for the hexagonal lattice parameter  $a$  or  $c$ , and  $p_{\text{LT}}$  and  $p_{\text{LN}}$  are the lattice parameters of pure LN and LT, respectively. The bowing parameter  $b$  for congruently grown crystals has been determined to be  $b = -0.03$  for the lattice parameter  $c$  and  $b = -0.007$  for the lattice parameter  $a$ . Using the commonly accepted values [35–38] of the hexagonal lattice parameters for congruent LN and LT, i.e.,  $a_{\text{LT}} = 5.1543 \text{ \AA}$ ,  $c_{\text{LT}} = 13.7835 \text{ \AA}$ ,  $a_{\text{LN}} = 5.1483 \text{ \AA}$ , and  $c_{\text{LN}} = 13.8631 \text{ \AA}$ , we have calculated the tantalum composition  $x$  in our crystals via Eq. (3).

The calculation is graphically displayed in Fig. 2(b). The red squares show the measured lattice parameters plotted with respect to the melt composition. The values are projected on Eq. (3) and yield the crystal composition  $x$  indicated by the blue circles. The confidence interval for the crystal composition  $x$  is estimated by projecting the confidence

TABLE II. Measured  $\text{LiNb}_{1-x}\text{Ta}_x\text{O}_3$  hexagonal lattice parameters with respect to the Ta concentration in the melt  $y$  and the actual Ta concentration in the crystals  $x$ .

Ta concentration in melt $y$	Ta concentration in crystal $x$	Lattice parameters	
		$c$ in $\text{\AA}$	$a$ in $\text{\AA}$
0.125	$0.261 \pm 0.02$	$13.837 \pm 0.002$	5.150
0.375	$0.553 \pm 0.04$	$13.812 \pm 0.003$	5.150
0.625	$0.839 \pm 0.06$	$13.793 \pm 0.004$	5.152
0.75	$0.841 \pm 0.03$	$13.792 \pm 0.002$	5.153
0.875	$0.967 \pm 0.03$	$13.785 \pm 0.002$	5.153

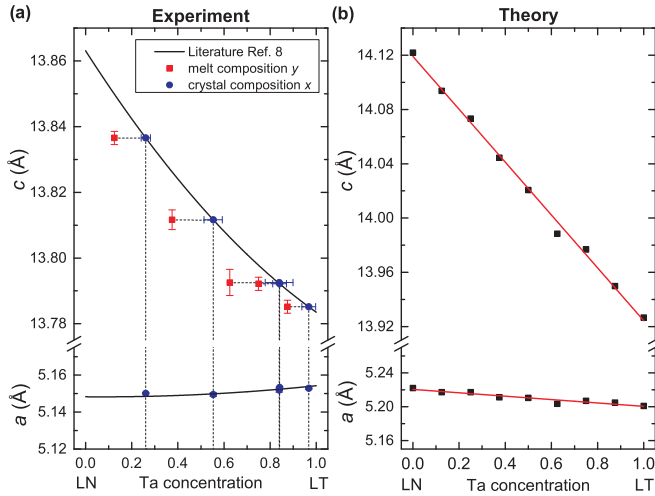


FIG. 2. (a) Measured and (b) DFT LNT lattice parameters as a function of the Ta concentration. The red squares are the measured lattice parameters plotted with respect to the melt composition  $y$ . The solid line shows the crystal composition  $x$  as extrapolated from Eq. (3).

interval of the XRD data for the parameter  $c$ . The results are summarized in Table II. The lattice parameter  $a$  agrees fairly well with the expected behavior. Its composition dependence is much less pronounced than in the case of the  $c$  parameter. The minor deviations from the literature behavior might be explained by different lithium content in the crystals, which has been previously shown to affect the lattice parameter [8,39].

The results obtained with the DFT models are shown in Fig. 2(b) and agree well with the experimental data. Our results clearly show that the lattice parameter  $c$  decreases with increasing Ta content. This can be explained partially by the smaller covalent radius of the fivefold coordinated Ta (1.46 Å) with respect to the covalent radius of the fivefold coordinated Nb (1.47 Å),<sup>1</sup> and partially by the shorter and stronger Ta-O bonds (1.997 Å on average) with respect to the Nb-O bonds (2.038 Å on average). The larger strength of the Ta-O bonds is corroborated by the  $\text{TO}_3$   $A_1$  phonon band only involving the Ta-O bond, which is harder in LT (348  $\text{cm}^{-1}$ ) than in LN (323  $\text{cm}^{-1}$ ).<sup>2</sup> In agreement with the measurements, a minor dependence of the lattice parameter  $a$  on the Ta concentration is calculated. Remarkably, the lattice parameter  $a$  is a slightly decreasing function of the Ta concentration in our simulations, while it is a slightly growing function of the Ta concentration in our measurements. This might be due to the higher Li deficiency in LN than in LT [14–16]. Indeed, the higher concentration of Li vacancies will reduce the effective lattice parameters in LN samples proportionally more than in LT samples [39]. While this effect is largely masked in the case of the parameter  $c$  due to the opposite and strong composition dependence, it becomes evident in the case of the parameter  $a$ , which shows a minor composition dependence.

Our calculations show a nearly perfect Vegard-like behavior for both lattice parameters with only a minor sign of bowing.

This is in agreement with the measurements of Bartasyte *et al.*, which showed that the bowing almost vanishes for nearly stoichiometric LNT crystals [8].

## B. Vibrational properties

With the knowledge of the crystal lattice parameters and the actual Ta concentration, the vibrational properties of the LNT samples can be studied by Raman spectroscopy and DFT. We discuss first the  $A_1$  modes and then the  $E$  modes. A brief overview of the calculated  $A_2$  phonons, which are neither Raman nor IR active, can be found in Sec. III C.

### 1. $A_1$ phonons

Figure 3 shows a typical Raman spectrum recorded in the  $x(z,z)\bar{x}$  scattering geometry. For better comparability, the spectra have been normalized to maximum after the dark count level was subtracted. The spectra have been separated with an artificial offset, which is proportional to the Ta ratio  $x$  in the crystal. As expected from group theory, four  $A_1$ -TO modes can be identified in all samples. These four modes, labeled  $A_1$ -TO<sub>1</sub> to  $A_1$ -TO<sub>4</sub>, are centered at 252, 273, 331, and 632  $\text{cm}^{-1}$  in LN and at 206, 252, 357, and 598  $\text{cm}^{-1}$  in LT. The measured wave numbers are in good agreement with previous studies [39–43].

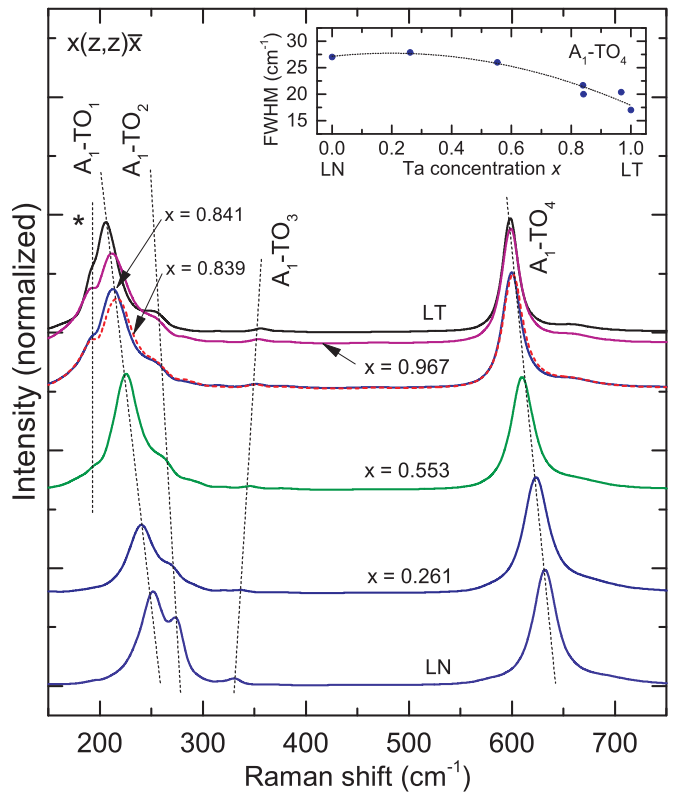


FIG. 3. Normalized Raman spectra obtained in  $x(z,z)\bar{x}$  scattering geometry showing the behavior of  $A_1$ -TO modes in  $\text{LiNb}_{1-x}\text{Ta}_x\text{O}_3$  mixed crystals. For better visibility, the spectra have been separated by an artificial offset proportional to the Ta content  $x$ . Four  $A_1$ -TO modes predicted by the theory can be identified in all spectra. The inset shows the measured FWHM of the  $A_1$ -TO<sub>4</sub> mode as a function of the Ta concentration, showing a clear decrease for Ta-rich crystals.

<sup>1</sup>Source: <https://www.webelements.com>.

<sup>2</sup>Values calculated from our DFT models.



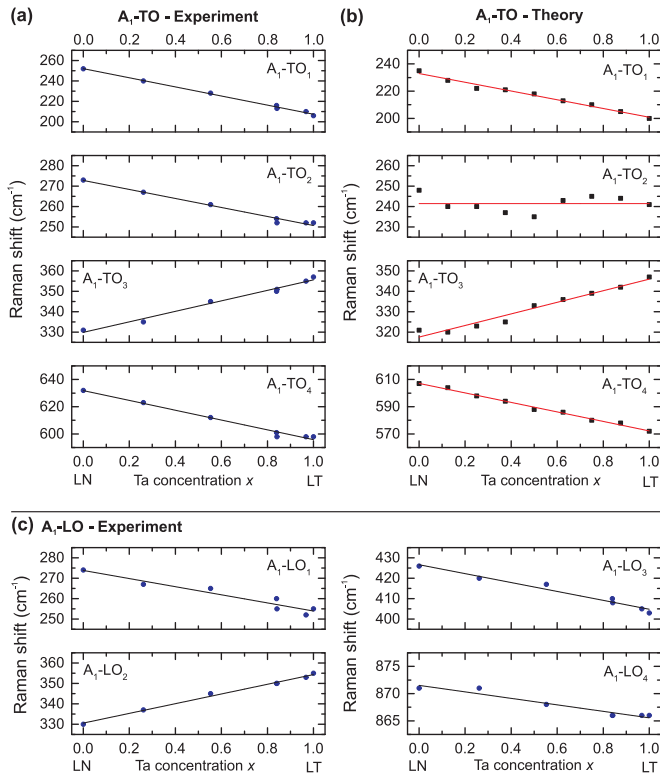


FIG. 4. Experimentally measured phonon frequencies of the  $A_1$ -TO modes as a function of the (a) Ta concentration  $x$  and (b) corresponding theoretical predictions. In (c), the experimental measured  $A_1$ -LO phonon frequencies are displayed, which are not covered by our model.

The spectra of the mixed crystals look very similar to the end compound spectra and also show four distinct  $A_1$  peaks.

The similarity of the spectra of mixed crystals and the end compounds is also observed for  $E$ -TO modes (see Fig. 6). The slight differences, mainly observed in  $A_1$ -TO<sub>1</sub> and -TO<sub>2</sub> peak shapes, are most likely due to differences in Li deficiency, which is known to affect both the peak position and FWHM of these modes [39,44]. The FWHM of the  $A_1$ -TO<sub>4</sub> is depicted in the inset in Fig. 3 and shows a clear decrease of the FWHM for higher Ta content. This behavior is also observed for other modes and suggests an overall better stoichiometry in Ta-rich crystals. Here, previous studies have established that the FWHM of most modes is proportional to the deviation from the ideal crystal stoichiometry [8,39].

The shift of the Raman peaks with the Ta content shown in Fig. 3 is displayed separately for each mode in Fig. 4(a) and compared with the outcome of the DFT calculations in Fig. 4(b). As a general feature, the phonon modes in LN have higher frequencies than the corresponding modes in LT. This can be easily understood as a result of the large mass difference between Nb (92.906 a.u.) and Ta (180.948 a.u.).<sup>3</sup> An exception is represented by the TO<sub>3</sub> phonon branch, which is a rigid rotation of the oxygen cage around the Nb (or Ta) atom (see Fig. 5). In this vibration, Nb (or Ta) atoms do not oscillate around their equilibrium positions so that no composition-dependent frequency shifts are expected due to atomic mass differences. It is rather the Nb-O or Ta-O bond strength that determines the mode energy. The shorter average Ta-O distance in LT (1.997 Å) with respect to the average Nb-O

<sup>3</sup>Source: <https://www.webelements.com>.

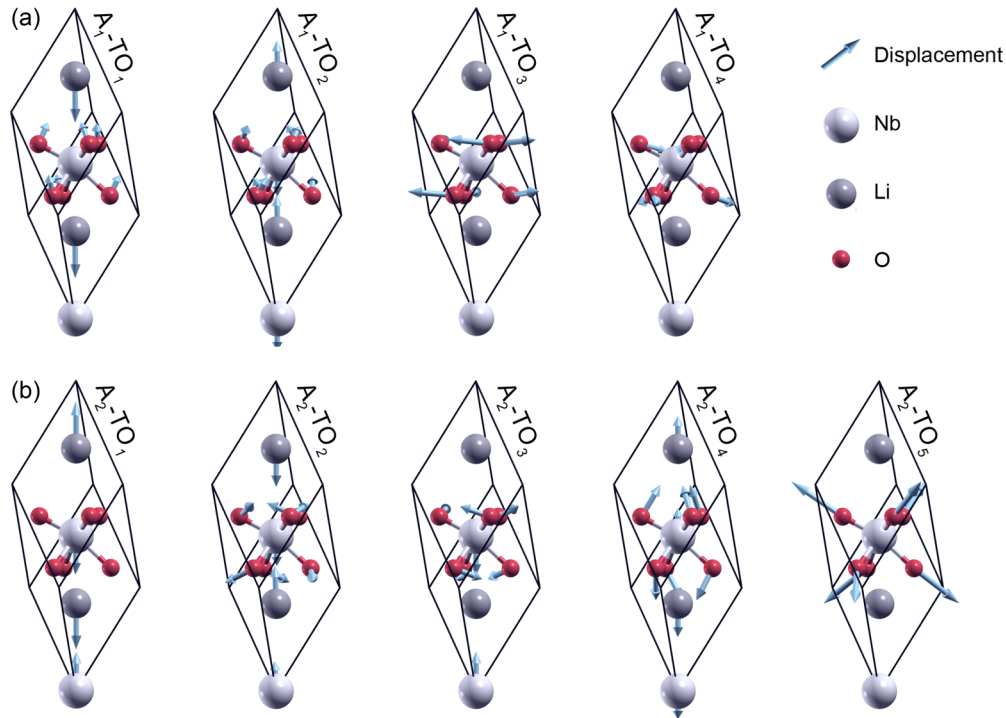


FIG. 5. Eigenvectors of the transversal phonon modes with (a)  $A_1$  symmetry and (b)  $A_2$  symmetry. Nb/Ta atoms are in white, Li in gray, and O in red. The arrows represent the atomic displacement direction.

distance in LN (2.038 Å) suggests a stronger Ta-O bond and explains the peculiar composition dependence of this mode.

Both measured and calculated data indicate a nearly Vegard-like behavior for all modes. The theoretical models predict both the direction and the magnitude of the composition-dependent frequency shift in very good agreement with the measured data for most modes. The only exception is represented by the  $A_1$ -TO<sub>2</sub> phonon branch, which shows a relatively large frequency shift ( $\Delta\bar{\nu} = \bar{\nu}_{LT} - \bar{\nu}_{LN} = -22 \text{ cm}^{-1}$ ) in the experiment, while the theory suggests no clear frequency shift over the compositional range. This deviation can be traced back, at least partially, to the presence of Li vacancies in the measured samples, which are neglected in our models. The  $A_1$ -TO<sub>2</sub> phonon mode is a vibration along the crystal  $z$  axis of the Li sublattice (see Fig. 5), and is therefore strongly affected by the presence of the  $V_{Li}$  vacancies and  $Nb_{Li}$  antisites occurring in the congruent samples. As this mode does not directly involve Nb or Ta atoms, it is expected to be relatively independent of the Nb/Ta ratio and to vibrate with similar frequencies in LN and in LT, as predicted by DFT. However, the amount of defects pinning the Li sublattice in LN is larger than in LT (larger deviation from the stoichiometry), so that the phonon is excited at higher energies in LN than in LT. Thus this mode appears harder in congruent LN samples than in congruent LT samples.

The experimental behavior of the  $A_1$ -LO phonons, which according to Table I can only be observed in the  $z(x,x)\bar{z}$  and  $z(y,y)\bar{z}$  geometries, is displayed in Fig. 4(c). The corresponding mode eigenvectors are shown in Fig. 5(b). Similarly to the  $A_1$ -TO phonons, a clear Vegard-like shift can be observed for all modes. Remarkably, the LO<sub>2</sub> and LO<sub>3</sub> modes show an opposite shift compared to the respective TO<sub>2</sub> and TO<sub>3</sub>, resulting in a larger LO-TO splitting in LT. As discussed in Sec. III D, this is connected to the different dielectric properties in LN and LT. In contrast to the other LO modes, the LO<sub>4</sub> phonon frequency shows a negligible composition dependence.

## 2. E phonons

Figure 6 shows a typical spectrum recorded in the  $x(y,z)\bar{x}$  scattering geometry, which allows for the detection of the  $E$ -TO modes. According to group theory, nine  $E$ -TO modes are expected for LNT crystals. However, only seven modes in LN and eight modes in LT can be unambiguously identified in our spectra, similarly to previous investigations [4,43,45]. A conclusive assignment of the Raman modes in LN and LT has only recently been achieved by low-temperature Raman analysis [43] and extensive theoretical investigations [4,45].

A comparison of the peak position and intensity with previous works and DFT models shows that the  $E$ -TO<sub>1</sub>, -TO<sub>2</sub>, -TO<sub>3</sub>, -TO<sub>4</sub>, -TO<sub>7</sub>, and -TO<sub>8</sub> are easily detectable in both materials. The broad spectral feature in the 350 to 400  $\text{cm}^{-1}$  range is actually built up by the overlap of the  $E$ -TO<sub>5</sub> and  $E$ -TO<sub>6</sub> modes and is, in principle, a double peak [43]. However, this peak can be clearly resolved only at low temperatures and in stoichiometric material. Our DFT calculations confirm that  $E$ -TO<sub>5</sub> and  $E$ -TO<sub>6</sub> have very similar energies and are separated by about 10  $\text{cm}^{-1}$ . According to our models, both modes do not involve Nb or Ta atoms (see Fig. 8) and consist mainly

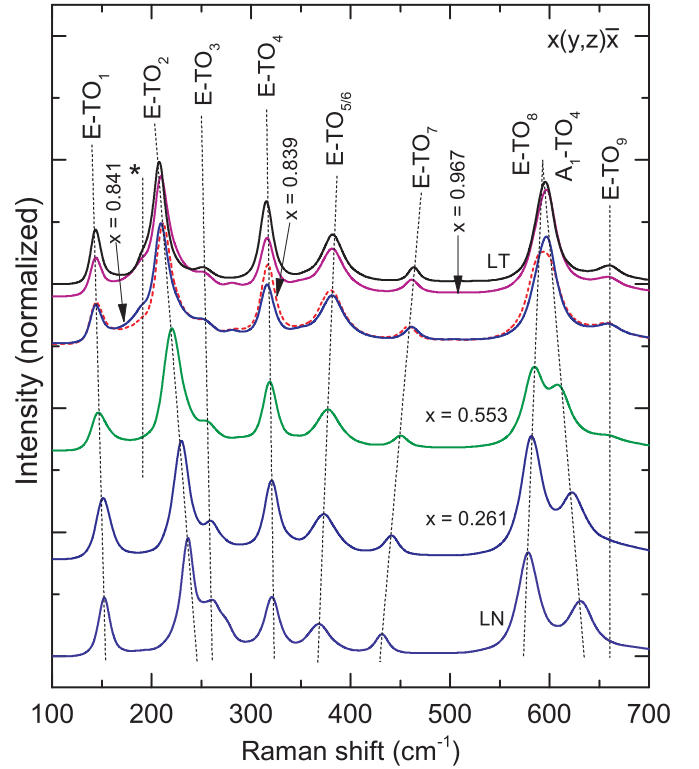


FIG. 6. Normalized Raman spectra obtained in the  $x(y,z)\bar{x}$  scattering geometry showing the  $E$ -TO modes in  $\text{LiNb}_{1-x}\text{Ta}_x\text{O}_3$  mixed crystals. The spectra have been separated with an artificial offset proportional to the Ta content  $x$ . Besides the  $E$  modes, an  $A_1$ -TO<sub>4</sub> leakage mode can be seen at high frequencies, resulting from an incomplete suppression of detection light. Peak assignment is carried following recent investigations [4,43,45].

of Li vibrations within the  $xy$  plane, which become harder with growing Ta concentration. The calculated frequency dependence on the Ta concentration is almost identical for the two peaks, as shown in Fig. 7(b). Correspondingly, we observe in Raman experiments a single peak, labeled  $E$ -TO<sub>5/6</sub>, which linearly shifts to higher frequencies with increasing Ta content without modifying its shape, in agreement with our theoretical model.

The other controversially discussed phonon mode is the  $E$ -TO<sub>9</sub> mode. In LT, this band is detected as a fairly intense peak at 660  $\text{cm}^{-1}$ , as shown in Figs. 6 and 11. The displacement pattern related to this phonon as calculated by DFT shows a distortion of the oxygen octahedra accompanied by minor cation displacements in the  $xy$  plane (see Fig. 8). The analysis of the LNT spectra reveals that the  $E$ -TO<sub>9</sub> peak intensity heavily depends on the Ta content, and becomes vanishing in LN (see Figs. 6 and 11). This is in very good agreement with previous work and theoretical models, which show that the scattering cross section of the  $E$ -TO<sub>9</sub> almost vanishes in LN, but is large in LT [4].

In Fig. 7, the experimentally obtained shifts are compared with our calculated values. Overall, the theoretical model predicts the observed behavior very well and the origin of the shifts can be interpreted in terms of the displacement patterns and the changing bonding conditions. The modes

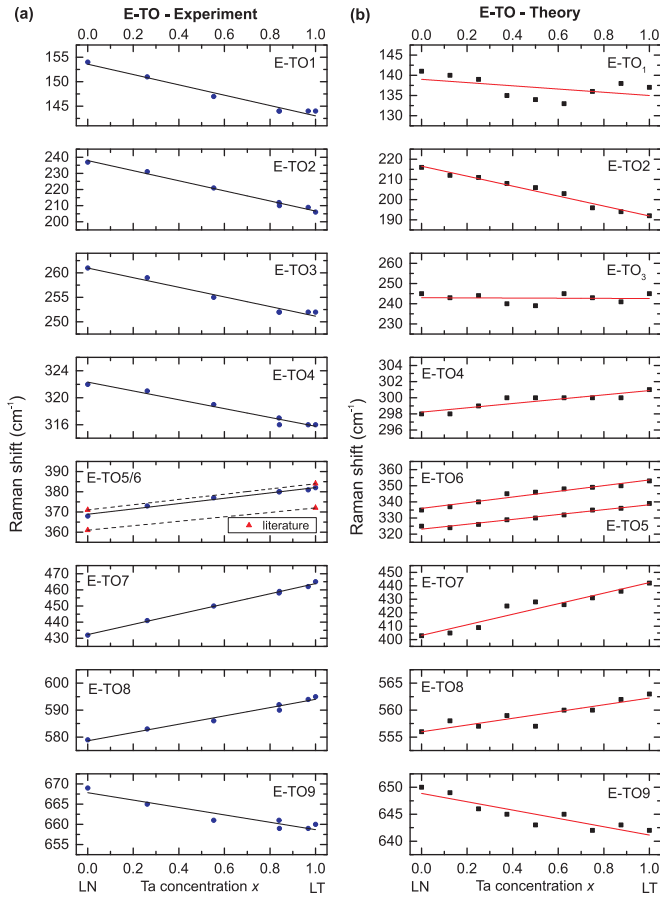


FIG. 7. Experimentally measured  $E$ -TO phonon frequencies in  $\text{LiNb}_{1-x}\text{Ta}_x\text{O}_3$  mixed crystals (a) as a function of the Ta concentration  $x$  and (b) comparison with the calculated values.  $E$ -TO<sub>5</sub> and  $E$ -TO<sub>6</sub> can only be resolved in low-temperature Raman spectroscopy [43]. Recent literature data of this resonance are shown for comparison [43].

$E$ -TO<sub>1</sub> and -TO<sub>2</sub> are deformations/tilting of the oxygen octahedra combined by cationic displacements in the  $xy$  plane. In agreement with the mass difference of Nb and Ta, the modes become softer with increasing Ta concentration.  $E$ -TO<sub>3</sub> is a tilting of the oxygen octahedra, whose composition dependence is slightly more pronounced in DFT than in the experiment.

The  $E$ -TO<sub>4</sub> mode is the only mode for which predicted and measured composition dependence of the phonon frequency is not in agreement. In the Raman experiment, it shows a slight decrease in frequency of  $\Delta \bar{\nu}_{E\text{-TO}_4} = -7 \text{ cm}^{-1}$  from LN to LT, while in DFT, the phonon energy slightly grows from LN to LT. Similarly to the  $A_1$ -TO<sub>2</sub> band discussed in Sec. III B 1, this is at least partially due to the different extent of Li deficiency in the LN and LT samples. Indeed, the mode is related to a movement in the antiphase of the cationic sublattice and is therefore strongly influenced by the Li deficiency.  $E$ -TO<sub>7</sub> and  $E$ -TO<sub>8</sub> are pure distortions of the oxygen octahedra not involving cationic displacement. Their growing frequency with Ta concentration can be understood in terms of stronger Ta-O bonds with respect to the Nb-O bonds.

The measured  $E$ -LO frequencies are displayed in Fig. 9. The  $E$ -LO modes can only be observed in the scattering

geometry  $y(x,x)\bar{y}$  and generally appear to be of weak intensity. Therefore, they are prone to overlapping by leakage modes and  $A_1$ -TO modes. In this work, the phonon assignment of the LO modes is performed following Ref. [43], in which the issues related to low-intensity peaks and leakage modes are thoroughly discussed. The  $E$ -LO<sub>4</sub> could not be detected with our experimental setup. It has an extremely weak intensity over the whole composition range, and can only be recorded at low temperatures and with a particular fitting procedure [43].

The  $E$ -LO<sub>2</sub> and  $E$ -LO<sub>7</sub> could not be detected for Ta concentrations higher than  $x > 0.261$ , due to the overlap with  $A_1$ -TO<sub>1</sub> and -TO<sub>2</sub> as well as  $E$ -TO leakage modes, respectively. The extrapolation of the measured data in this composition range displayed in Fig. 9 fits well with Raman measurements on LT from Margueron *et al.* [43], which we plot in the same figure for comparison.

### C. Further spectral features

So far we have discussed the behavior of the first-order Raman peaks. Besides these first-order bands, we observe several yet unassigned spectral features, which we briefly discuss in this chapter. The unassigned peaks are observed at frequencies lower than  $200 \text{ cm}^{-1}$  and higher than  $600 \text{ cm}^{-1}$ . In the low-frequency range, we can distinguish two structures appearing in different scattering configurations. First, in the spectra collected with incident light from the  $z$  direction, we detect a weak feature between the  $E$ -TO<sub>1</sub> and  $E$ -TO<sub>2</sub> modes, which is exemplarily shown in Fig. 10 for the  $z(y,x)\bar{z}$  scattering geometry. A broad band centered at approximately  $190 \text{ cm}^{-1}$  is observed in LN, which shifts to lower frequencies with increasing Ta content (about  $160 \text{ cm}^{-1}$  in LT). The second low-frequency feature is detected for incident light along the  $x$  or  $y$  direction, as shown in Figs. 3 and 6, highlighted with an asterisk. Here, a peak centered at  $190 \text{ cm}^{-1}$  can be seen, which is only detected in the Ta-rich samples ( $x \geq 0.553$ ). This peak shows no apparent shift, but shows an increase in intensity for Ta-rich samples, which has been detected in previous studies as well [40,43]. Regarding its intensity behavior, this peak has some similarity to another unassigned peak detected over the complete compositional range in LNT crystal, which is centered at  $740$  to  $750 \text{ cm}^{-1}$ , as depicted in Fig. 11(a). This band is only detected for incident light from the  $z$  direction and becomes particularly strong in LT. In the past, some authors have considered this peak to be a fundamental mode, e.g., the missing  $E$ -TO<sub>9</sub> mode [40]. As of today, the aforementioned features are considered to be results of the two-phonon process, which explains their pronounced temperature dependence [42,46] and stoichiometric sensitivity [42]. Hence, these features appear more intense in the Ta-rich samples [14–16], which are closer to stoichiometric composition than LN samples (see Sec. III B 1).

Probably the most remarkable of these unassigned features is a band which appears for incident light from the  $z$  direction in pure LN as a fairly broad feature centered at approximately  $620 \text{ cm}^{-1}$ . This is depicted in Fig. 11(b). In several previous works, this band has been identified as the missing  $E$ -TO<sub>9</sub> in LN [35,42,47]. Indeed, this feature has been found to become sharper in nearly stoichiometric material [35,42] and lies above  $600 \text{ cm}^{-1}$ , where the  $E$ -TO<sub>9</sub> is expected according to

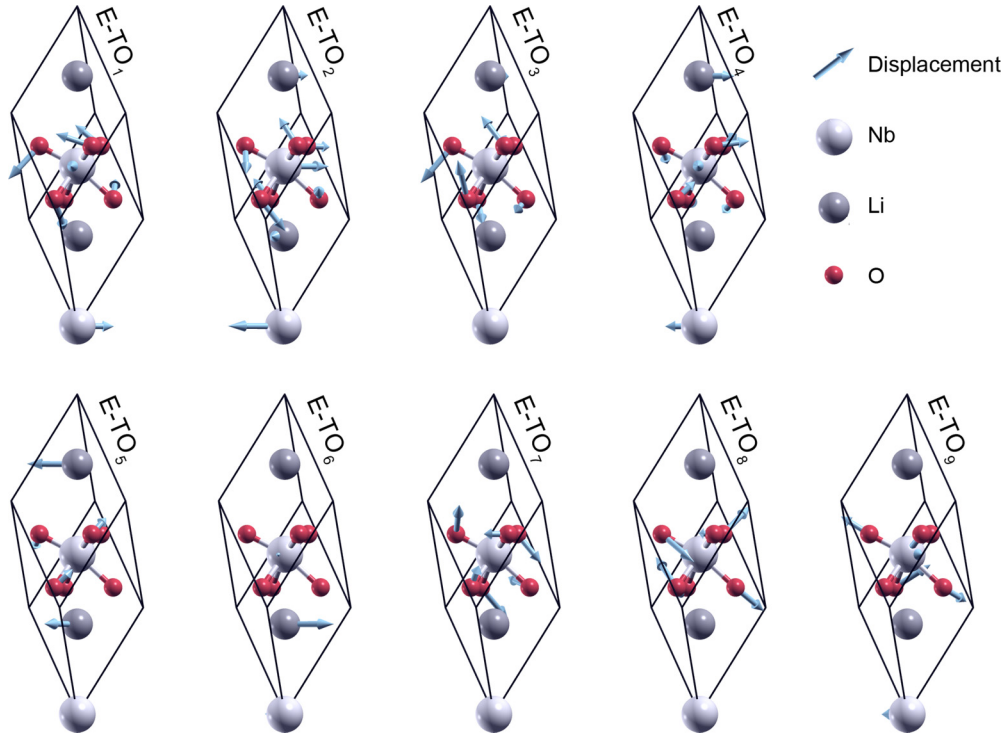


FIG. 8. Eigenvectors of the transversal phonon modes with  $E$  symmetry. Arrows represent the atomic displacement direction; color coding as in Fig. 5.

theoretical models and IR spectroscopy [45,48]. The intensity of this band has been found to be very sensitive to ferroelectric domain walls and is applied for visualization of ferroelectric domain structures by confocal Raman imaging [22,49–51]. Interestingly, this band is not observed in LT. Here, apparently only fundamental modes are found to be sensitive to domain

structures. Therefore, the origin of this additional feature in LN and its behavior in mixed crystals is of particular interest for the interpretation of confocal Raman data. As shown in

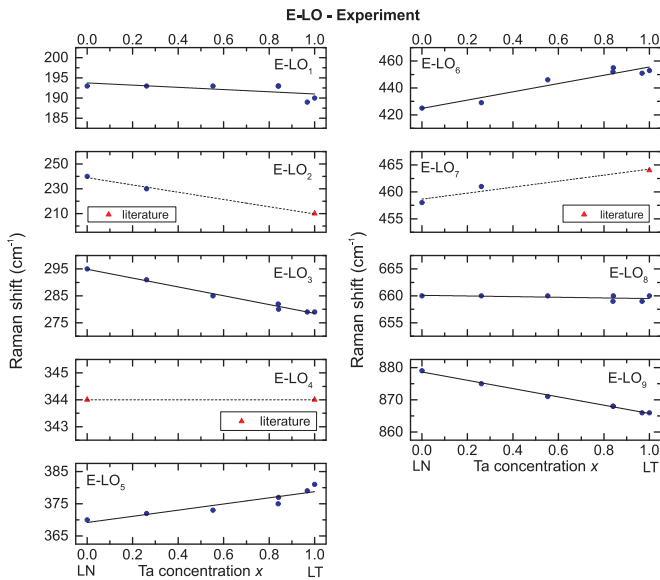


FIG. 9. Experimentally measured  $E$ -LO phonon frequencies in  $\text{LiNb}_{1-x}\text{Ta}_x\text{O}_3$  mixed crystals as a function of the Ta concentration  $x$ .  $E$ -LO modes can only be detected in a single scattering configuration and are weak in intensity. For the sake of completeness, our results are complemented by recent literature data [43].

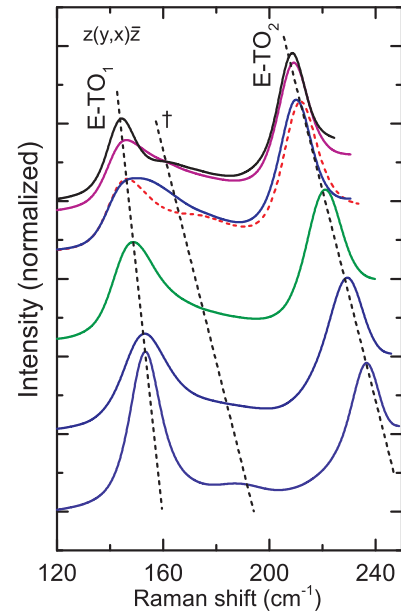


FIG. 10. Detailed view of the frequency range between the  $E$ -TO<sub>1</sub> and  $E$ -TO<sub>2</sub> modes. A broad structure shifting to lower frequencies on Ta-rich samples is labeled by a dagger. This spectral feature is related to a two-phonon process and heavily depends on stoichiometry [42,46]. Small variations in stoichiometry explain the slightly varying shapes obtained for different compositions.



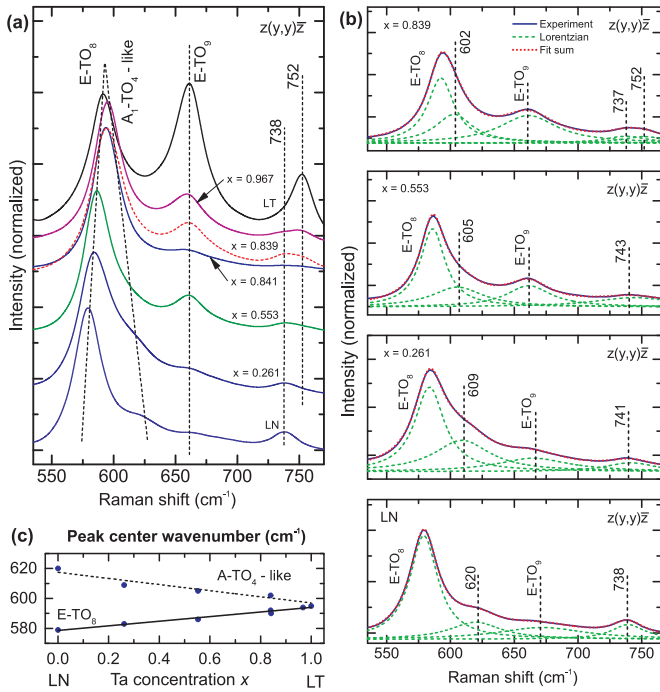


FIG. 11. (a) Closeup of the spectral range from 535 to 770  $\text{cm}^{-1}$  in  $z(y,y)\bar{z}$ . The spectra have been normalized to the  $E\text{-TO}_8$  mode intensity to warrant comparability. (b) Lorentzian fits of the represented spectral range, which highlight the shift of the features in the 600–620  $\text{cm}^{-1}$  range. (c) Shift of the central frequency of the  $E\text{-TO}_8$  and possible  $A_1\text{-TO}_4$ -like mixed mode.

Fig. 11, this band shifts to lower frequencies and can be identified up to  $x = 0.839$  samples by fitting the spectra. At higher Ta concentrations, it merges with the  $E\text{-TO}_8$  band in LT, which directly explains the apparent absence of such a feature in LT. This observation is in good agreement with the peculiar response of the  $E\text{-TO}_8$  intensity to ferroelectric domain walls in LT compared to LN [49]. Apparently, the response of the  $E\text{-TO}_8$  in LT to domain walls is moderated by the superimposed response of the  $E\text{-TO}_8$  and the so-far unassigned feature. Remarkably, this additional band shows a very similar shift as the  $A_1\text{-TO}_4$  mode, but is measured at slightly lower frequencies. We suggest this band to be a mixed mode propagating at oblique angles, but with mainly  $A_1\text{-TO}_4$  character. This  $A_1\text{-TO}_4$ -like mode is excited and detected by leakage effects due to a  $k$ -vector distribution in the focused laser beam [52,53]. Such an origin explains why various authors have observed the center of this band in a fairly broad frequency range (610–630  $\text{cm}^{-1}$ ) [35,42,47]. Indeed, the detection and peak shape might depend on the experimental setup, i.e., the objective lens (numerical aperture) and its illumination. Its  $A_1\text{-TO}_4$ -like character also explains the high sensitivity for ferroelectric domain walls [22] and the strong connection to the stoichiometry of the material [42].

The  $A_2$  phonon modes are characterized by displacement patterns that preserve the crystal symmetry, similarly to the  $A_1$  modes discussed in Sec. III B 1. However, differently from the latter, atoms of the same type vibrate in antiphase and do not modify the crystal polarization. Thus,  $A_2$  phonon modes are Raman and IR silent and cannot be detected with our experimental setup. Nonetheless, they show a frequency

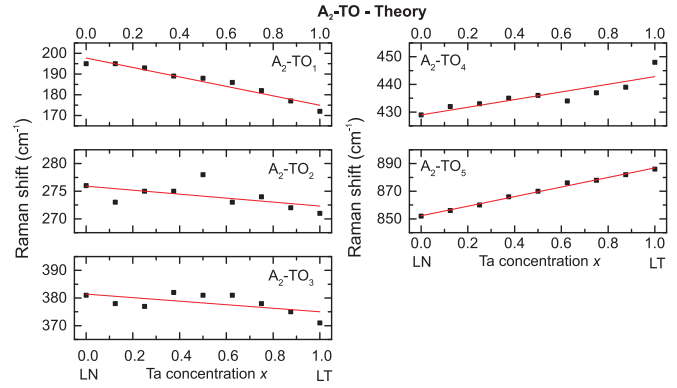


FIG. 12. Calculated frequencies of the  $A_2$  phonons with respect to Ta concentration  $x$ .

dependence on the Ta concentration, which we have calculated by DFT. The resulting eigenvectors are shown in Fig. 5 and the frequency shifts are shown in Fig. 12. While  $A_2$   $\text{TO}_1$ ,  $\text{TO}_2$ , and  $\text{TO}_3$  involve vibrations of Ta or Nb ions along the  $z$  axis and decrease their frequency with the Ta concentration,  $A_2$   $\text{TO}_4$  and  $\text{TO}_5$  represent breathing modes of the oxygen cage (accompanied by a  $z$  vibration of the Li sublattice in the case of  $\text{TO}_4$ ) and increase their frequency with growing Ta concentration.

#### D. Dielectric properties of mixed crystals

While the high-frequency dielectric function can be calculated within the density functional theory as a sum over electronic empty states (once the electronic ground state is known), the phononic contribution to the material's optical response must be estimated with more refined and computationally demanding approaches [54]. One way to estimate the phononic contribution to the dielectric tensor in an approximate way is given by the well-established Lyddane-Sachs-Teller (LST) relation [55]. In its generalized form [56], the LST relation reads

$$\varepsilon_0 = \varepsilon_\infty \cdot \prod_j \left( \frac{\omega_{\text{LO}}^j}{\omega_{\text{TO}}^j} \right) \quad (4)$$

and connects the frequencies of all LO and TO phonons ( $\omega_{\text{LO}}^j$  and  $\omega_{\text{TO}}^j$ ) with the static and high-frequency permittivity ( $\varepsilon_0$

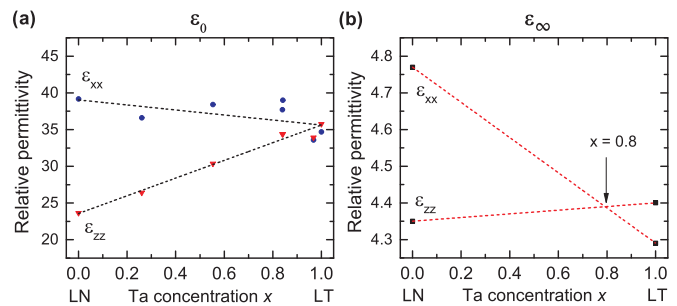


FIG. 13. The compositional dependence of the static dielectric permittivity estimated by Eq. (4). The extraordinary permittivity  $\varepsilon_{zz}$  shows a strong dependence on the Ta content, while the ordinary permittivity  $\varepsilon_{xx}$  is almost constant.

TABLE III. Summary of the high-frequency and static permittivity calculated for the end compounds LN and LT, respectively. The obtained values are in good agreement with the literature [43,47,57–60].

	$\epsilon_0$		$\epsilon_\infty$	
	This work	Literature	This work	Literature
$\epsilon_{xx}$ (LN)	$39.2 \pm 5.7$	40.2–42.5	4.77	5.0
$\epsilon_{zz}$ (LN)	$23.6 \pm 1.8$	23.7–26	4.35	4.6
$\epsilon_{xx}$ (LT)	$34.7 \pm 5.2$	39.6–42	4.29	4.50
$\epsilon_{zz}$ (LT)	$35.8 \pm 2.7$	35.9–40	4.40	4.53

and  $\epsilon_\infty$ ) of the material. The dielectric tensor of crystals with the  $C_{3v}$  symmetry has only two different components and is given by

$$\epsilon = \begin{pmatrix} \epsilon_{xx} & 0 & 0 \\ 0 & \epsilon_{xx} & 0 \\ 0 & 0 & \epsilon_{zz} \end{pmatrix}. \quad (5)$$

Thereby,  $\epsilon_{xx}$  is the tensor component along the crystallographic  $x$  and  $y$  direction, while  $\epsilon_{zz}$  is the tensor component along the  $z$  direction. We have calculated the static permittivity  $\epsilon_0$  for LNT crystals using the previously determined phonon frequencies. The high-frequency permittivity in mixed crystals is calculated from hybrid DFT. In particular,  $\epsilon_\infty$  is calculated for LN and LT. The calculated values are shown in Fig. 13(b) for the two tensor components. For LN, the calculation yields values of  $\epsilon_{xx} = 4.77$  and  $\epsilon_{zz} = 4.35$ , while for LT, we obtain  $\epsilon_{xx} = 4.29$  and  $\epsilon_{zz} = 4.40$ . The calculated values slightly underestimate the experimental values [57,58], as summarized in Table III, but can be considered in good agreement with the experimental data. In particular, our theoretical approach correctly predicts the existence of an optically isotropic material with vanishing birefringence. In order to estimate the value of the high-frequency dielectric constant for the exact Ta concentration in the samples, we linearly interpolate the calculated values.

Within the described approach, we obtain permittivity values for the end components LN and LT, which are in good agreement with literature values, as summarized in Table III. The calculated values for the  $\text{LiNb}_{1-x}\text{Ta}_x\text{O}_3$  mixed

components are plotted in Fig. 13(a). Our data suggests a Vegard-like behavior with no pronounced bowing. The ordinary permittivity  $\epsilon_{xx}$  shows only a slight decrease with increasing Ta content, while the extraordinary dielectric constant  $\epsilon_{zz}$  grows linearly from about  $\epsilon_{zz} = 23.7$  in LN to  $\epsilon_{zz} = 35.8$  in LT. For high-Ta concentrations, our data suggest an almost optically isotropic crystal, which is in good agreement with previous reports [43,47,57–60]. Our data clearly show that the optical isotropy observed for high (or optical) frequencies is also observed in the static regime.

#### IV. CONCLUSION

In this work, lithium niobate tantalate mixed crystals have been Czochralski grown over the complete compositional range. The structural properties of the obtained crystals have been studied by XRD measurements, while their vibrational properties have been investigated by Raman spectroscopy and density functional theory. The calculated composition dependence of the phonon frequencies describes well the measured behavior. Furthermore, the relation between Raman frequency shift and crystal stoichiometry can be explained on the basis of the phonon eigenvectors. Although most modes become softer with growing Ta concentration (as expected considering the Nb and Ta atomic mass), a few modes not involving the Nb or Ta atoms become harder with growing Ta concentration. The knowledge of the phonon frequencies is exploited to calculate the ordinary and extraordinary static dielectric function of the mixed crystals. Our data suggest a Vegard-like behavior of the static permittivity and an almost optically isotropic crystal for high-Ta concentrations, similarly to the crystal's optical response in the high-frequency regime. The tunability of the optical response makes lithium niobate tantalate mixed crystals a promising functional material for application in integrated optics.

#### ACKNOWLEDGMENTS

The authors acknowledge the Deutsche Forschungsgemeinschaft (DFG) for financial support by the SFB/TRR 142. All of the calculations were performed at the Paderborn Center for Parallel Computing (PC<sup>2</sup>) and at the High Performance Computing Center in Stuttgart (HLRS).

- 
- [1] *Physics of Ferroelectrics, A Modern Perspective*, Topics in Applied Physics, Vol. 104, edited by K. M. Rabe, C. H. Ahn, and J.-M. Triscone (Springer-Verlag, Berlin Heidelberg, 2007).
  - [2] *Ferroelectric Materials and their Applications*, edited by Y. Xu (Elsevier, Amsterdam, 1991).
  - [3] R. S. Weis and T. K. Gaylord, *Appl. Phys. A* **37**, 191 (1985).
  - [4] S. Sanna, S. Neufeld, M. Rüsing, G. Berth, A. Zrenner, and W. G. Schmidt, *Phys. Rev. B* **91**, 224302 (2015).
  - [5] R. D. Shannon, *Acta Crystallogr. Sect. A* **32**, 751 (1976).
  - [6] K. Sugii, H. Koizumi, S. Miyazawa, and S. Kondo, *J. Cryst. Growth* **33**, 199 (1976).
  - [7] F. Shimura and Y. Fujino, *J. Cryst. Growth* **38**, 293 (1977).
  - [8] A. Bartasyte, A. M. Glazer, F. Wondre, D. Prabhakaran, P. A. Thomas, S. Huband, D. S. Keeble, and S. Margueron, *Mater. Chem. Phys.* **134**, 728 (2012).
  - [9] F. Shimura, *J. Cryst. Growth* **42**, 579 (1977).
  - [10] I. G. Wood, P. Daniels, R. H. Brown, and A. M. Glazer, *J. Phys. Condens. Matter* **20**, 235237 (2008).
  - [11] D. Xue, K. Betzler, and H. Hesse, *Solid State Commun.* **115**, 581 (2000).
  - [12] A. Riefer, S. Sanna, and W. G. Schmidt, *Ferroelectrics* **447**, 78 (2013).

- [13] S. Sanna, A. Riefer, S. Neufeld, W. G. Schmidt, G. Berth, M. Rüsing, A. Widhalm, and A. Zrenner, *Ferroelectrics* **447**, 63 (2013).
- [14] P. Lerner, C. Legras, and J. P. Dumas, *J. Cryst. Growth* **3-4**, 231 (1968).
- [15] J. R. Carruthers, G. E. Peterson, M. Grasso, and P. M. Bridenbaugh, *J. Appl. Phys.* **42**, 1846 (1971).
- [16] R. L. Barns and J. R. Carruthers, *J. Appl. Cryst.* **3**, 395 (1970).
- [17] W. D. Johnston, Jr. and I. P. Kaminow, *Phys. Rev.* **168**, 1045 (1968).
- [18] M. Friedrich, A. Riefer, S. Sanna, W. G. Schmidt, and A. Schindlmayr, *J. Phys. Condens. Matter* **27**, 385402 (2015).
- [19] M. Friedrich, A. Schindlmayr, W. G. Schmidt, and S. Sanna, *Phys. Stat. Sol. B* **253**, 683 (2015).
- [20] R. F. Schaufele and M. J. Weber, *Phys. Rev.* **152**, 705 (1966).
- [21] S. Sanna, G. Berth, W. Hahn, A. Widhalm, A. Zrenner, and W. G. Schmidt, *Ferroelectrics* **419**, 1 (2011).
- [22] G. Berth, W. Hahn, V. Wiedemeier, A. Zrenner, S. Sanna, and W. G. Schmidt, *Ferroelectrics* **420**, 44 (2011).
- [23] G. Kresse and J. Fürthmüller, *Phys. Rev. B* **54**, 11169 (1996).
- [24] J. P. Perdew and Y. Wang, *Phys. Rev. B* **33**, 8800 (1986).
- [25] J. P. Perdew, J. A. Chevary, S. H. Vosko, K. A. Jackson, M. R. Pederson, D. J. Singh, and C. Fiolhais, *Phys. Rev. B* **46**, 6671 (1992).
- [26] P. E. Blöchl, *Phys. Rev. B* **50**, 17953 (1994).
- [27] F. D. Murnaghan, *Proc. Natl. Acad. Sci. USA* **30**, 244 (1944).
- [28] J. Heyd, G. E. Scuseria, and M. Ernzerhof, *J. Chem. Phys.* **118**, 8207 (2003).
- [29] A. V. Krukau, O. A. Vydrov, A. F. Izmaylov, and G. E. Scuseria, *J. Chem. Phys.* **125**, 224106 (2006).
- [30] J. P. Perdew, K. Burke, and M. Ernzerhof, *Phys. Rev. Lett.* **77**, 3865 (1996).
- [31] Y. Li, S. Sanna, and W. G. Schmidt, *J. Chem. Phys.* **140**, 234113 (2014).
- [32] Y. Li, W. G. Schmidt, and S. Sanna, *Phys. Rev. B* **89**, 094111 (2014).
- [33] Y. Li, W. G. Schmidt, and S. Sanna, *Phys. Rev. B* **91**, 174106 (2015).
- [34] A. Riefer, S. Sanna, A. Schindlmayr, and W. G. Schmidt, *Phys. Rev. B* **87**, 195208 (2013).
- [35] Y. Repelin, E. Husson, F. Bennani, and C. Proust, *J. Phys. Chem. Solids* **60**, 819 (1999).
- [36] S. C. Abrahams, E. Buehler, W. C. Hamilton, and S. J. Laplaca, *J. Phys. Chem. Solids* **34**, 521 (1973).
- [37] S. C. Abrahams, J. M. Reddy, and J. L. Bernstein, *J. Phys. Chem. Solids* **27**, 997 (1966).
- [38] Y. S. Kim and R. T. Smith, *J. Appl. Phys.* **40**, 4637 (1969).
- [39] M. D. Fontana and P. Bourson, *Appl. Phys. Rev.* **2**, 040602 (2015).
- [40] X. Yang, G. Lan, B. Li, and H. Wang, *Phys. Stat. Sol. B* **142**, 287 (1987).
- [41] A. F. Penna, A. Chaves, P. da R. Andrade, and S. P. S. Porto, *Phys. Rev. B* **13**, 4907 (1976).
- [42] A. Ridah, P. Bourson, M. D. Fontana, and G. Malovichko, *J. Phys. Condens. Matter* **9**, 9687 (1997).
- [43] S. Margueron, A. Bartaszyte, A. M. Glazer, E. Simon, J. Hinka, I. Gregora, and J. Gleize, *J. Appl. Phys.* **111**, 104105 (2012).
- [44] F. Abdi, M. D. Fontana, M. Aillerie, and P. Bourson, *Appl. Phys. A* **83**, 427 (2006).
- [45] P. Hermet, M. Veithen, and P. Ghosez, *J. Phys. Condens. Matter* **19**, 456202 (2007).
- [46] A. Ridah, M. D. Fontana, and P. Bourson, *Phys. Rev. B* **56**, 5967 (1997).
- [47] I. P. Kaminow and W. D. Johnston, Jr., *Phys. Rev.* **160**, 519 (1967).
- [48] V. Caciuc, A. V. Postnikov, and G. Borstel, *Phys. Rev. B* **61**, 8806 (2000).
- [49] G. Stone and V. Dierolf, *Opt. Lett.* **37**, 1032 (2012).
- [50] V. Y. Shur and P. S. Zelenovskiy, *J. Appl. Phys.* **116**, 066802 (2014).
- [51] P. Capek, G. Stone, V. Dierolf, C. Althouse, and V. Gopalan, *Phys. Stat. Sol. C* **4**, 830 (2007).
- [52] R. Ossikovski, Q. Nguyen, G. Picardi, J. Schreiber, and P. Morin, *J. Raman Spectrosc.* **39**, 661 (2008).
- [53] S. Röhrig, C. Krautgasser, R. Bermejo, J. L. Jones, P. Supancic, and M. Deluca, *J. Eur. Ceram. Soc.* **35**, 4321 (2015).
- [54] A. Riefer, M. Friedrich, S. Sanna, U. Gerstmann, A. Schindlmayr, and W. G. Schmidt, *Phys. Rev. B* **93**, 075205 (2016).
- [55] R. H. Lyddane, R. G. Sachs, and E. Teller, *Phys. Rev.* **59**, 673 (1941).
- [56] A. S. Chaves and S. P. S. Porto, *Solid State Commun.* **13**, 865 (1973).
- [57] A. S. Barker, Jr., A. A. Ballman, and J. A. Ditzenberger, *Phys. Rev. B* **2**, 4233 (1970).
- [58] A. S. Barker, Jr. and R. Loudon, *Phys. Rev.* **158**, 433 (1967).
- [59] *Properties of Lithium Niobate*, edited by K. K. Wong (IET, London, 2002).
- [60] T. Fujii, A. Ando, and Y. Sakabe, *J. Eur. Ceram. Soc.* **26**, 1857 (2006).